PUBLICATIONS OF THE ASTRONOMICAL SOCIETY OF THE PACIFIC, **118**:21–36, 2006 January

Exploring the Potential of Integral Field Spectroscopy for Observing Extrasolar Planet Transits: Ground-based Observations of the Atmospheric Na in HD 209458b

SANTIAGO ARRIBAS,[1,2,3,4] RONALD L. GILLILAND,[1] WILLIAM B. SPARKS,[1] LUIS LÓPEZ-MARTÍN,[3] EVENCIO MEDIAVILLA,[3] AND PEDRO GÓMEZ-ALVAREZ[3]

Received 2005 July 5; accepted 2005 September 5; published 2006 January 10

ABSTRACT. We explore the use of integral field spectroscopy (IFS) for observing extrasolar planet transits. Although this technique should find its full potential in space-based observations (e.g., *James Webb Space Telescope*, *Terrestrial Planet Finder*), we have tested its basics with ground-based time-series observations of HD 209458b obtained with the William Herschel Telescope optical fiber system INTEGRAL during a transit in 2004 August 17/18. For this analysis we have used 5550 spectra (from a potential of ~30,000) obtained in 150 exposures during a period of more than 7 hr. We have found that IFS offers three fundamental advantages with respect to previously used methods (based on imaging or standard slit spectroscopy). First, it improves the effective signal-to-noise ratio in photon-limited observations by distributing the light coming from the star into the two dimensions of the detector. Second, this type of IFS data allows us to "autocalibrate" instrumental and background effects. Third, since the star image characteristics (i.e., seeing, spatial shifts, etc.) as well as its photometric properties are extracted from the same data cube, it is possible to decorrelate photometric instabilities induced by point-spread function (or instrument) variations. These data have also allowed us to explore the accuracy limits of ground-based *relative* spectrophotometry. This was done using a photometric index that probes the Na D lines, for which we obtained a nominal 1 σ error of $\sim 1.0 \times 10^{-4}$. This result, based on observations of only one transit, indicates that this type of ground observation can constrain the characterization of the transmission spectrum of extrasolar planets, especially if they cover multiple transits under good weather conditions. The present observations are compatible with no extra Na D depression during the transit. Although this result seems to be inconsistent with the recently reported *Hubble Space Telescope* STIS findings, we point out its limited statistical meaning: the results disagree within 1 σ, but agree within 2 σ. This method requires careful and specific reductions, and details about this process are given. We also give some recommendations to instrument developers in order to enhance the efficiency of the method.

Online material: color figure

1. INTRODUCTION

The transit method (TM) has recently gained much attention among the various methods of detecting extrasolar planets, due to its potential for discovering Earth-like planets. This method also offers the possibility for studying the existence of planetary satellites, rings, and atmospheric features (see, e.g., Deeg 2002). All these possibilities have been clearly demonstrated with HD 209458, the first planetary transit discovered (Charbonneau et al. 2000; Henry et al. 2000; Mazeh et al. 2000). The light curve of this object has allowed for an unprecedented characterization of the star/planet system (e.g., planetary and stellar radii, stellar limb darkening, orbital inclination, period, etc.), imposing limits to the presence of planetary satellites and rings (Brown et al. 2001), and detecting features associated with the planetary atmosphere (Charbonneau et al. 2002; Vidal-Madjar et al. 2003, 2004). Recently, Deming et al. (2005) have reported the detection of mid-infrared radiation from the planet by observing the decrement in flux during secondary eclipse, when the planet passes behind the star.

The success of the TM largely relies on the (spectro)photometric accuracy with which the light curve can be obtained. For some science applications (e.g., detection of planetary atmospheric features), only accurate *relative* spectrophotometry [i.e., band1/(nearby)band2 and in/out transit] is required, drastically reducing systematic correlated errors that may otherwise limit the signal-to-noise ratio (S/N). Experiments with the *Hubble Space Telescope* (*HST*; Gilliland et al. 1999; Brown et al. 2001; Gilliland & Arribas 2003) have demonstrated that accuracies of $\sim 10^{-5}$ or higher can be reached from space.

Such a high accuracy is not always required. For instance,

[1] Space Telescope Science Institute, 3700 San Martin Drive, Baltimore, MD 21218.

[2] Affiliated with the Space Telescope Division of the European Space Agency, ESTEC, Noordwijk, Netherlands.

[3] Instituto de Astrofísica de Canarias, 38200 La Laguna, Tenerife, Spain.

[4] Consejo Superior de Investigaciones Científicas (CSIC), Spain.

in the wavelength domain 1190–1710 Å, Lyα, O I, and C II lines suffer a drop of ~15%, 13%, and 7.5%, respectively, during the transit (Vidal-Madjar et al. 2003, 2004). In optical wavelengths, the variations are indeed smaller. Charbonneau et al. (2002) have found a drop of 2.5 parts in 10,000 (i.e., 0.025%) in the Na D resonant lines during the transit. This drop is smaller than expected from (poorly constrained) models, which also predict that other spectral characteristics in the optical (e.g., Rayleigh continuum) should be detected with lower accuracies (e.g., Brown 2001). The smaller than expected Na D absorption detected by Charbonneau et al. (2002) may have resulted from a high cloud deck, a low atomic Na abundance, or a combination of these.

In this context, it is relevant to understand the accuracy limits that can be achieved from the ground. This should allow us to know if parts of future studies could be performed by taking advantage of the more abundant and flexible observing time available from ground-based observatories, or if we need to rely entirely on space data. Note that with the advent of large-aperture ground-based telescopes, the Poisson limit may be boosted, allowing access to more numerous and distant systems. This is particularly relevant to follow-up observations of planetary transits discovered by missions such as *Kepler* (Borucki et al. 2004). Pioneering ground-based attempts to detect spectral features due to the planetary atmospheres in 51 Peg and HD 209458 include Coustenis et al. (1998), Rauer et al. (2000), Bundy & Marcy (2000), Moutou et al. (2001), and Brown et al. (2002). More recently Deming et al. (2005), using NIRSPEC on the Keck II telescope, have reported upper limits to the CO absorption at a sensitivity level that suggests that a general masking mechanism is present in the planetary atmosphere of HD 209458b. In addition, Narita et al. (2005) have recently studied the transmission spectrum of this object, on the basis of high-resolution spectroscopy with the Subaru High Dispersion Spectrograph (HDS). Although the accuracy of these observations were unable to confirm or contradict the results of Charbonneau et al. (2002), they reported upper limits on absorption due to several optical transitions. All these ground-based observations have gained importance since the *HST* Space Telescope Imaging Spectrograph (STIS) became inoperative.

In this paper we propose to take advantage of the comprehensive collecting nature of IFS to perform this type of observation. This observational method, whose advantages are described in § 2, is tested with ground-based data. The observations are described in § 3. Details about the reduction process for this particular application are described in § 4. The results are shown and discussed in § 5, while § 6 summarizes the main conclusions. Although this paper is focused on the potential of IFS for observing extrasolar planet transits, the reader may also be interested in other closely related applications of IFS (e.g., Arribas et al. 1998a; Sparks & Ford 2002).

2. PROPOSED METHOD: THE POTENTIAL OF IFS IN OBSERVATIONS OF PLANET TRANSITS

Gilliland et al. (1999) proposed to increase the photometric accuracy of very high S/N observations by using the spectroscopic mode of STIS. By distributing the starlight along the dispersion direction, it is possible to increase the total number of photons collected before the detector reaches the saturation limit. This simple idea enhances the duty cycle of the instrument (i.e., total number of photons by unit of available time, including overheads), which translates to an increase in the S/N when the photon noise is the major source of noise. The larger detector footprint of the stellar light has negligible consequences in terms of adding noise in a very high S/N regime. In fact, it has the beneficial effect of averaging out flat-field and sensitivity residuals. Another practical advantage is the possibility of defining a posteriori ad hoc "filters" that are well suited for the science applications.

Here we propose to extend this idea by means of integral field spectroscopy (IFS). Thanks to the two-dimensional to one-dimensional conversion performed by a fiber bundle (or by an image slicer), the starlight is spread not only along the dispersion direction, but also across dispersion. This technique allows us to use a larger area of the detector, boosting the limit imposed by the photon noise per exposure. Note that to optimize the use of the detector, the image of the star at the focal plane should be well oversampled by the integral field unit (IFU). Since for these transit observations we are interested in the total number of photons recorded in a limited period of time (i.e., duration of the transit), the image at the input of IFU could be defocused (or it could even be the pupil image). Note that defocusing the star image on the IFU does not modify the spectral resolution of the observations, which is another practical advantage of the IFS method over previous spectroscopic methods.

The ability to distribute the light over the whole detector is particularly relevant with the advent (and prospects) of very large telescopes. This can be easily understood from the following example. Typical imaging observations of HD 209458b ($V = 7.64$) in a 100 Å band with an 8 m telescope will saturate in ~0.1 s. Given a typical readout time of 60 s, and taking into account that the transit lasts ~3 hr, an effective integration time of ~20 s on the source during the transit could be obtained. If the observations were done with a standard slit spectrograph working at 1 Å pixel^{-1}, saturation would be roughly reached in ~10 s, and the effective integration time would be ~30 minutes. If the observations were done with an IFS at the same spectral resolution, and sampling the (defocused) star image with 100 spatial elements ("spaxels") on the IFU, the effective exposure time could be increased by up to 2.8 hr (out of 3 available). Of course, real observations can be optimized by defining faster readouts, modifying the spectral resolution, etc. Detectors such as that used by ULTRACAM (Dhillon &

Marsch 2002) may also reduce overheads. The numbers above are just illustrative of current standard detectors.

Apart from the ability to gather photons, stability is crucial for TM observations. Of course, beyond some limits it is not possible to control the stability of the environment and/or the observational setup. While this is true for both space- and ground-based observations, the unstable nature of the Earth's atmosphere makes very accurate ground observations particularly challenging. In any case, when uncontrolled instabilities may affect the photometric accuracy of the system, a good record of the instabilities may make it possible to decorrelate the photometric signal. This provides another important advantage of the IFS. Since both the spectra from which the photometric information is obtained *and* the images of the object (point-spread functions; PSFs) are extracted from the same data cube, we can remove photometric variations induced by PSF instabilities. Furthermore, in a fiber-based IFS (and to a lesser degree a slice-based IFU), a shift of the image on the focal plane may be well tracked independently of a shift between the pseudoslit and the detector. This gives full control of the PSF variations, as well as optical and mechanical shifts during time-series observations. Fiber systems also provide a series of generic advantages, such as the azimuthal scrambling of the light (which reduces errors in the barycenter of the recorded fiber image), the possibility of using static spectrographs (which reduces flexure-induced errors), etc. (for more details, see Arribas & Mediavilla 2000). On the other hand, apart from the extra light losses induced by the IFU, potential problematic aspects of fiber-based IFS systems include the modal noise due to small changes in fiber position or illumination (e.g., Baudrand & Walker 2001), and a possible temporal variation of the fiber throughput with wavelength. However, we see below that at least for the present instrumental configuration, our data do not suggest that these potential problems contribute significantly to the noise.

Another advantage of IFS for these types of observations is a consequence of the large number of spectra collected simultaneously, which can be used to *autocalibrate* the data themselves from detector and background signatures. This is shown in § 5.

In summary, IFS provides three main advantages for transiting planet observations: (1) it improves the ability to collect photons during the transit, enhancing the S/N, (2) it allows the user to autocalibrate the data, and (3) by independently tracking the instabilities produced at the focal plane and those due to the spectrograph, it is possible to remove noise in the photometric signal correlated to these PSFs and instrumental instabilities.

3. OBSERVATIONS

We performed the observations with the 4.2 m William Herschel Telescope (WHT) during 2004 August 17/18 using the INTEGRAL system (Arribas et al. 1998b) connected to WYFFOS (Wide Field Fiber Optic Spectrograph; Bingham et al. 1994). We used the recently installed WYFFOS long camera, equipped with two EEV-42-80 thinned and coated CCDs joined along their long axis to provide a 4K × 4K pixel mosaic. The high-speed readout mode (45 s) was used, with gains of 2.3 e^- (chip1-red) and 1.94 e^- (chip2-blue), yielding a readout noise of 6 e^-. These detectors are considered linear for standard observations up to ~52,000 ADU (see below). Note that WYFFOS is mounted on one of the Nasmyth platforms of the WHT, which provides good mechanical stability (see below).

The fiber bundle SB1 (standard bundle 1), consisting of 205 fibers, each 0.″45 in diameter, was used. This bundle is arranged such that 175 fibers cover a rectangular area of 7.″8 × 6.″4, while 30 additional fibers forming a 90″ diameter concentric ring around the rectangle simultaneously measure the sky background. The actual distribution of the fibers at the focal plane can be found in Figure 6 of Arribas et al. (1998b), and also in Figure 1 of del Burgo et al. (2000).

We used the R316R (316 line mm^{-1}) grating, which gives an effective resolution of ~3 Å and covers the ~4000–10000 Å spectral range.

INTEGRAL does not have an independent focus mechanism for the fiber bundles, so the only way to spread the light over the input of the fiber bundle in a controlled way is to defocus the telescope. However, we decided not to apply any major defocus to the telescope, because it would have affected the guiding quality.

The observations on target consisted of eight time series of 20 individual exposures of 120 s each (the eighth series had to be suspended after 10 individual exposures were taken, because of a detectable flux increase due to the twilight). After each time series, we took a short flat-field exposure. Therefore, the total object data set consisted of 150 individual exposures (with a potential of ~30,000 individual spectra, although of course many had low S/N) extending for a period of more than 7 hr, from which 5 hr were integrating on the target. The weather conditions were good, with a stable seeing of ~0.″8. The values of atmospheric extinction in the visible (r' band) obtained by the Carlsberg Meridian Telescope[5] also suggest stable and photometric conditions for the night, with a mean value for the extinction coefficient of 0.091 ± 0.011 mag per air mass, using data spanning a period of 4 hr. Nonphotometric data were not detected for this night.

We located the object slightly off-center (i.e., around fiber number 111 in the standard code for this bundle), in order to minimize the effects of a broken fiber located in the opposite direction. The "central fiber," or "fiber 111," is the fiber closest to the peak of the image in most of the exposures. The 37 fibers around it covered most of the target flux.

Apart from lamp flats taken between sets of 20 exposures, bias, wavelength calibration, and sky flat images for calibration

[5] See http://www.ast.cam.ac.uk/~dwe/SRF/camc_extinction.html.

purposes were taken at the beginning and at the end, during the twilight. The internal calibration illumination does not mimic the exit pupil of the telescope; it produces slightly larger fiber images. This should be irrelevant, given the use of the these calibration images for the present application (see § 4).

4. REDUCTIONS

The reductions of these IFS data have the goal of generating both spectra (from which the relative spectrophotometric index is derived) and images (from which PSF characteristics are obtained) for each of the 150 individual exposures. Here we briefly describe the steps followed during this process, commenting on the relative importance of each step for this particular application.

4.1. Spectral Reductions

The present study focuses on the analysis of the Na D lines. As mentioned in § 1, these lines have been studied with great accuracy using the *HST* (Charbonneau et al. 2002), which provided us with a good reference to compare against the present observations. For this reason, and with the aim of simplifying and making the reduction process more manageable, we trimmed our original images into a spectral region of ~200 Å, including the above-mentioned resonant lines.

4.1.1. Bias

The bias value was obtained from the overscan strips signal. For the red chip used here, the mean value in that region increased linearly over the night from 1018 to 1028 ADU. The rms of this relation is about $\lesssim$1 ADU, a very small value compared to the typical signal of the brightest spectrum (~40,000 ADU). This indicates that the expected errors associated with an incorrect bias subtraction should have a minimal effect on the relative photometry of these very high S/N observations.

4.1.2. Flat-Field Correction

By construction, in many IFS systems it is not possible to directly illuminate the detector with a uniform source (e.g., blank sky). This is due to the presence of the IFU (i.e., fiber bundle, image slicer, microlens array) in the optical path, which prevents the user from directly obtaining flat fields for correcting pixel-to-pixel sensitivity variations. Instead, "flats" usually refer to images obtained when uniformly illuminating the input of the IFU, sometimes called "flat spectra." These are generally used to correct differences in throughput among the different sampling elements (i.e., fibers), and also sensitivity variations of *extracted pixels*. Note that an extracted pixel is generally obtained by integrating several individual pixels across the dispersion direction, so they represent an averaged (weighted) behavior. Although this approach is generally enough for most applications, in some cases it may represent a limitation. We show below that our spectra drift by about 0.6 detector pixels during the 7.5 hr of the observations, so different pixel sensitivities could emulate object flux variations.

Although it is not possible to obtain direct detector flats with INTEGRAL/WYFFOS, its detector is used at the prime focus of the WHT for direct imaging. Fortunately, this detector was used for several imaging programs during 2004 September, so we collected the flats recorded during this period (kindly provided to us by D. Lennon) to create a very high S/N "superflat." For the spectral range considered here, we combined about 40 images (mostly in the *V* filter) and corrected them from low spatial frequency variations using the IRAF tasks `imcombine` and `flat1d`. Note that although relatively large fringing amplitudes have been measured at longer wavelengths ($\lambda > 7000$ Å), the wavelength range analyzed in this paper is free of that effect. This superflat has about 10^6 ADU ($2.3 \times 10^6\ e^-$) and therefore a nominal S/N pixel^{-1} of ~1500.

4.1.3. Linearity Correction

The photometric index at a given time is obtained after averaging the individual values obtained from the spectra recorded at that particular time. The fact that the relative intensity of these individual spectra may change during the night (due not only to guiding and seeing instabilities, but also to the unavoidable differential atmospheric diffraction), makes the spectral index sensitive to detector linearity deviations.

The linearity of the present detectors was studied by Tulloch (2001). We have fit a polynomial function to his experimental data, with signals $\lesssim$38,000 ADU (rms of 0.14%). For signals >38,000 ADU, the slope of the linearity curve changes sharply from its relatively smooth behavior at lower signals. This slope change is difficult to model in detail, so we decided not to correct for this linearity slope change (i.e., we apply a constant correction for values >38,000 ADU). Linearity corrections at the lower signal end (i.e., <1000 ADU) are also difficult to model with high accuracy, but effects on the relative photometry are small. In § 5, we analyze and correct for the residuals of this linearity correction.

4.1.4. Extraction

The detector readout noise has a minimal effect in these very high S/N observations, we therefore decided to use relatively wide extraction windows of 14 pixels. This width guarantees the collection of most of the flux from a fiber/spectrum, but still avoids overlapping information from different spectra. In addition, taking into account the relatively small drift of the spectra in cross dispersion over the night (~0.6 pixels in 7.5 hr), we decided to use a fixed extraction window for all the spectra/exposures. (However, we also reduced the data, allowing for global shifts in the location of the extraction windows, but no appreciable changes were detected.) The functions defining the

centers of the extraction windows were obtained by adjusting polynomials to the spectra of the image obtained by adding all the flat-lamp exposures (after previous removal of the cosmic rays). It was verified that these spectra were actually located near the mean position during the night. These functions were fifth-degree polynomials obtained after fitting 130 data points along the selected spectral range. Typical rms were of 0.015 pixels (no significant improvement was found when using higher degree polynomials). The extraction was done as a simple summation (i.e., not with PSF shape and inverse variance weighting) in order to avoid undesired renormalization factors, which could affect the flux. Although these factors should have a very small effect on standard observations, it is possible that they may have some relevance for the current ultraprecise photometry. Therefore, we decide not to use this approach, which also has very little advantage in a high-S/N regime. In any case, we checked to ensure that no relevant differences were found when an optimal extraction was performed.

4.1.5. Wavelength Calibration

For the present analysis, the wavelength calibration is important to accurately define the bands used for creating the spectral index. Although the absolute conversion from pixels to wavelength coordinates does not need to be particularly accurate, it is important to correct any drift or change of the wavelength solution among fibers, especially during the night.

To obtain the absolute wavelength calibration for each fiber, we used the wavelength calibration exposures obtained for such a purpose. That was done using as a reference the brightest spectrum with the IRAF task `calibrate`. The individual wavelength solutions for each fiber were then obtained with `recalibrate`. To detect any drift along the dispersion direction, we cross-correlated the three brightest spectra in the images obtained through the night. These spectra are located in the region of the detector where most of the signal is extracted. We find a similar behavior in the three cases, with a linear shift of ~0.3 pixels over the night at a constant rate of ~0.04 pixel hr^{-1}, with a typical rms of 0.05 pixels. Therefore, to improve the accuracy of the drift associated with each exposure, we combined all the spectra obtained in a given exposure, and cross-correlated these integrated spectra.

Once the wavelength solution (and spectral drift) was known, we decided not to resample the individual spectra to a common spectral range and dispersion. This step would have implied an extra interpolation of the data. We found it preferable to use this information to homogeneously define the spectral bands of all the spectra (see § 5.2). The wavelength solution was applied with the IRAF task `dispcor`.

4.1.6. Cosmic-Ray Rejection

The cosmic-ray (CR) rejection is an important step in the reductions, since a relatively small number of carelessly removed cosmic rays could substantially degrade the S/N of the data. After trying several automatic rejection methods, we decided that none of these methods was sufficiently reliable for our particular case. The reason for this is that because the spectra are well separated on the detector, slight shifts of the image at the focal plane may produce relatively important changes in the flux at the detector, which may be interpreted as a CR when different exposures are compared. Therefore, we decided to follow the secure method of removing the CR in an interactive manner. In order to identify more easily cosmic rays, each individual spectrum was divided by a high-S/N, clean template, so even if a CR hits in the middle of the spectral feature (i.e., the Na D lines), it could be removed reliably. After the cosmic rays were identified and removed, the spectra were multiplied by the template. A total of ~80 cosmic rays were identified and removed in the relevant spectral range, but of course the full set of over 5000 spectra were inspected.

4.1.7. Throughput Correction

Flat-field spectra were applied to correct for fiber sensitivity. This was done using the blank sky observations made during the twilight at the beginning and end of the night. Although the fiber-to-fiber sensitivity variations are large (rms ~20%), these are stable during the night, with typical differences of less than ~1% (i.e., the difference of two flats taken at the beginning and end of the night gave a rms of 1.1% for the 37 fibers used, which probably imposes an upper limit to the actual fiber throughput stability). Note that global fiber sensitivity variations have no impact on the determination of spectral indices, which always probe relative flux variations (i.e., band1/band2). A temporal variation in the fiber throughput with wavelength could be a limitation, but we do not have evidence for such a behavior. (As we show in § 5, changes in the throughput-wavelength function seem to be dominated by atmospheric more than by instrumental effects.)

Although the photometric index is not dependent of the correction of fiber throughputs, this affects the star image reconstruction. In fact, errors in the fiber throughput corrections may produce incorrect PSF reconstruction, introducing further uncertainties during the decorrelation process. The throughput correction may also affect the background subtraction. However, in these two cases, the effects on the final results are very small (see below).

4.1.8. Background Subtraction

As described in § 3, 30 fibers located in a ring 90″ in diameter around the star allowed us to obtain contemporaneous background information. The spectra of some of these fibers are located relatively close to fibers with very high signals, so they may be affected by cross talk (or scattered light). Therefore, the averaged value of only 18 of these fibers was actually used to obtain the background information.

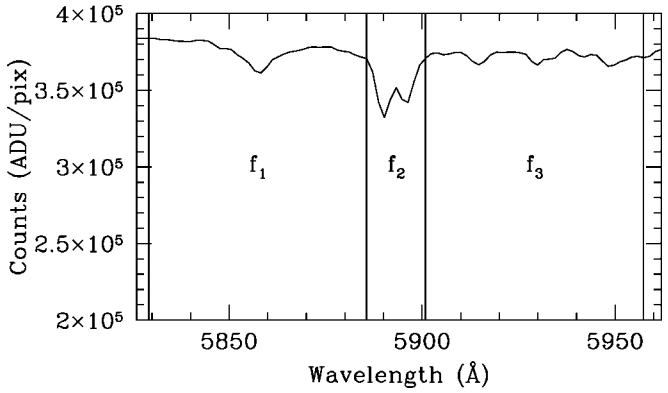

FIG. 1.—Spectrum generated after combining all the reduced spectra obtained in a single 120 s exposure. Vertical lines indicate the boundaries of the different bands used for the definition of the photometric index (see text).

Figure 1 shows a typical integrated spectrum obtained in an exposure after combining all the individual reduced spectra obtained for each fiber.

4.2. Reconstructed Images

In order to obtain the star images, we created files with the *X* and *Y* positions of the fibers in the focal plane of the telescope, and the integrated (background-subtracted) flux in the range 5829.200–5957.321 Å used for the definition of the photometric index in § 5 (i.e., $f_t = f_1 + f_2 + f_3$). With the help of the Numerical Algorithm Group routine `E01SAF`, an interpolating two-dimensional surface $F(x, y)$ is generated. This routine guarantees that the constructed surface is continuous and has continuous first derivatives. The interpolant $F(x, y)$ was then evaluated regularly each 0.″05 with the routine `E01SBF` on a grid of 80 × 80 pixels to create the maps presented here. Only 37 fibers were considered to have enough signal for the definition of the photometric index (see § 5.2), and these were also the ones used for the generation of the images. (They cover a hexagon centered on the fiber closest to the image peak). Figure 2 shows an example of such a reconstruction. A visual inspection of these images immediately allowed us to identify the loss of lock in the guiding system for four exposures, something confirmed later by the keywords in the headers of these images.

The images were adjusted to two-dimensional Gaussians with the help of the IRAF task `n2gaussfit`. It is well known that the seeing function does not fit a Gaussian in the outer parts (wings). Therefore, we restrict these fits to a relatively small box of 0.″8 (the estimated seeing). As a result of these fits, we obtained the evolution of the following parameters: position (*X*, *Y*; position with respect to the central fiber), FWHM (semimajor axis), amplitude, ellipticity, and P.A. of the major axis. Note that for this particular application, we are not interested in the absolute value of these variables (which depend on assumptions about the function assumed), but only on their relative evolution through the night.

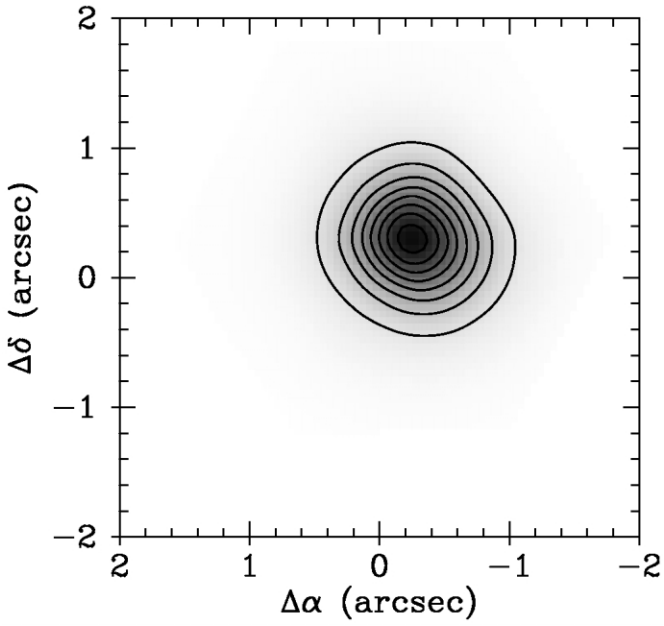

FIG. 2.—Reconstructed image of the star at the focal plane during a typical 120 s exposure (see text).

5. RESULTS

5.1. Auxiliary Variables

We selected a set of auxiliary variables that were compared through the night with the photometric index defined in § 5.2. These variables were obtained from the ING meteorological database, from the reduced spectra, and from the reduced images. As noted above, an important advantage of the IFS (especially the optical fiber approach) is the possibility to independently track the variations produced at the focal plane of the spectrograph (due, for instance, to instabilities of the mechanical structures, changes in the spectrograph focus, etc.), and those produced at the telescope focal plane (seeing changes, guiding instabilities, sky level variations, etc.). Figures 3–5 show the changes of these variables across the night.

In Figure 3 we show the change in air temperature, humidity, atmospheric pressure, sky level, and air mass. In this figure we can see that the object was well located on the sky for these observations, and we could observe it for more than 7 hr at an air mass lower than 2. The sky background level was somewhat unstable at the beginning of the night. In four images, there was a relatively sudden drop (∼+100 minutes, in the timescale of the figure), but it was later discovered that for these images, we lost the guiding system, so it was a spurious result (deviant results from these images were also found for other variables; see below). The background has a general trend of decreasing over the night. The last two points in the panel

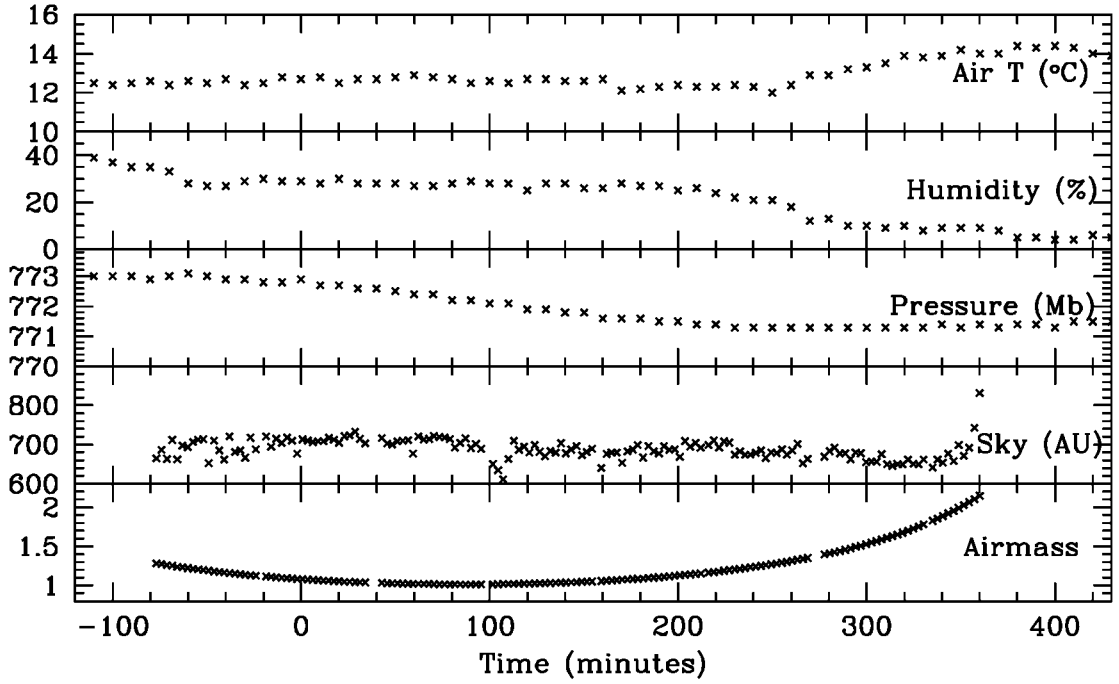

FIG. 3.—Evolution of some atmospheric variables during the night (see text). Units for the horizontal axis are in minutes from the center of the transit. AU refers to arbitrary units.

indicate the increase due to the twilight. The values for the air temperature (T), humidity, atmospheric pressure, and wind intensity (not shown) indicate that the night had good, stable conditions. Measurements of the seeing outside the dome were below 0.″8 most of the night.

Figure 4 shows a set of variables inferred from the spectra. The two lower panels illustrate the drifts of the spectra during the night along and across the dispersion directions (due to the motion of the image of the pseudoslit with respect to the detector). We can see that the spectra move at a relatively constant rate of 0.08 pixel hr^{-1} (across) and 0.03 pixel hr^{-1} (along). Although these are very small changes, drifts of the spectra over the night make the observations sensitive to flat-field corrections and the extraction aperture location. We did not find appreciable relative motion among the spectra, nor global rotation. Figure 4 also shows the evolution of the FWHM of the spectra integrated over the central band of the index (i.e., f_2; see below). This also shows a small monotonic change during the first part of the night, reaching a stable value for the second part of the night. The two deviant points ($t \sim +100$ m) correspond to the images taken when the guiding system was lost (the relative change in the spectral intensity produces a small but appreciable change in the FWHM). The variable denoted ΔFWHM represents the relative change in the FWHM between the line (f_2) and the continuum (f_1, f_3) bands used for the definition of the index, as explained below. The variation of the total flux integrated over the 37 fibers and over the total spectral range used for the definition of the photometric index (i.e., $f_1 + f_2 + f_3$) is also represented, together with the individual f_1, f_2, and f_3 fluxes. As we show below, the variation of these fluxes is clearly correlated with the star position in the bundle, the seeing, and the air mass. Finally, the top panel represents the ratio of the two continua used in the definition of the index (i.e., f_1/f_3).

Figure 5 shows how the variables obtained after fitting the reconstructed images with a simple two-dimensional Gaussian model change over the night. This figure shows a slight drift of the star image over the fiber bundle (~0.″4) during the first 3 hr, until the point at which the autoguiding was lost; it remains relatively constant the rest of the night. These panels also show a clear correlation between the ellipticity and the FWHM, and an anticorrelation of these two variables with the amplitude of the Gaussian fit and total flux. This behavior is expected, due to the fact that under these good seeing conditions, the fiber bundle undersamples the PSF.

5.2. Index Definition

We define a photometric index probing the Na D lines as

$$I = \frac{f_1 - f_2 + f_3}{f_1 + f_2 + f_3}, \tag{1}$$

where f_1, f_2, and f_3 represent the sky-subtracted flux (on a scale of photoelectrons) in the following spectral ranges: 582.9200–

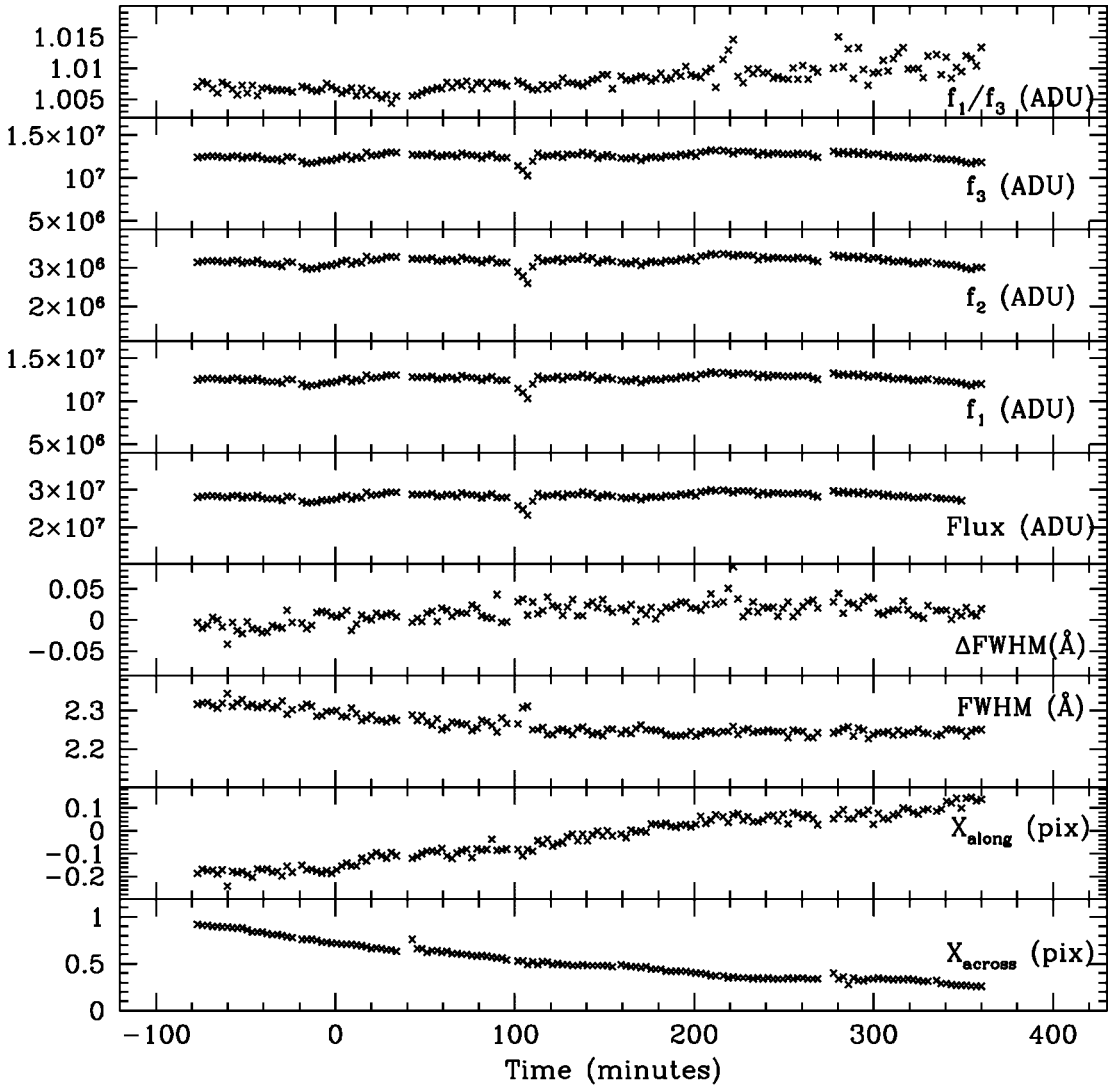

FIG. 4.—Evolution of some variables inferred from the spectra during the night (see text). *Bottom to top*: (1) Drift of the spectra in cross dispersion, (2) shift of the spectra along the spectral direction, (3) FWHM of the spectra, (4) variation of the FWHM between the line and continua bands, (5) total flux contained in the 37 spectra considered for the definition of the photometric index and for the reconstruction of the images, (6)–(8) the corresponding individual fluxes for bands f_1, f_2, and f_3, and (9) ratio f_1/f_3. Units for the horizontal axis are in minutes from the center of the transit. ADU refers to counts on the detector.

588.5643, 588.5643–590.0887, and 590.0887–595.7321 nm, respectively. Therefore, the Na D feature is well centered within f_2, while f_1 and f_3 represent symmetrical blue and red continua, respectively. Note that this index is insensitive to global (i.e., gray) variations in the flux. Also note that by increasing the width of bands f_1 and f_3 (and assuming stable continuum values), one would reduce the standard deviation of a distribution of index values. This apparent gain in accuracy is obviously compensated for by the fact that the index is less sensitive to changes in f_2. Therefore, once the width of f_1 and f_3 are large enough relative to f_2 (so that the statistical noise fixing the continuum is small compared to that due to f_2), no real gain is obtained by increasing the width of those bands (and furthermore, systematic errors can be introduced).

As defined in equation (1), the index I will probe the Na D lines under the assumption that f_1 and f_3 are stable continua. Charbonneau et al. (2002) have reported a very stable continuum around the Na D lines, so one could only expect temporal variation of f_1 and f_3 due to instrumental or atmospheric conditions. Some authors (e.g., Winn et al. 2004, and references therein) have found relatively large time-dependent instrumental (blaze function) variations, which were interpreted as being caused by flexure of the spectrograph. However, in the present case, our fiber-fed spectrograph is mounted on a stable platform,

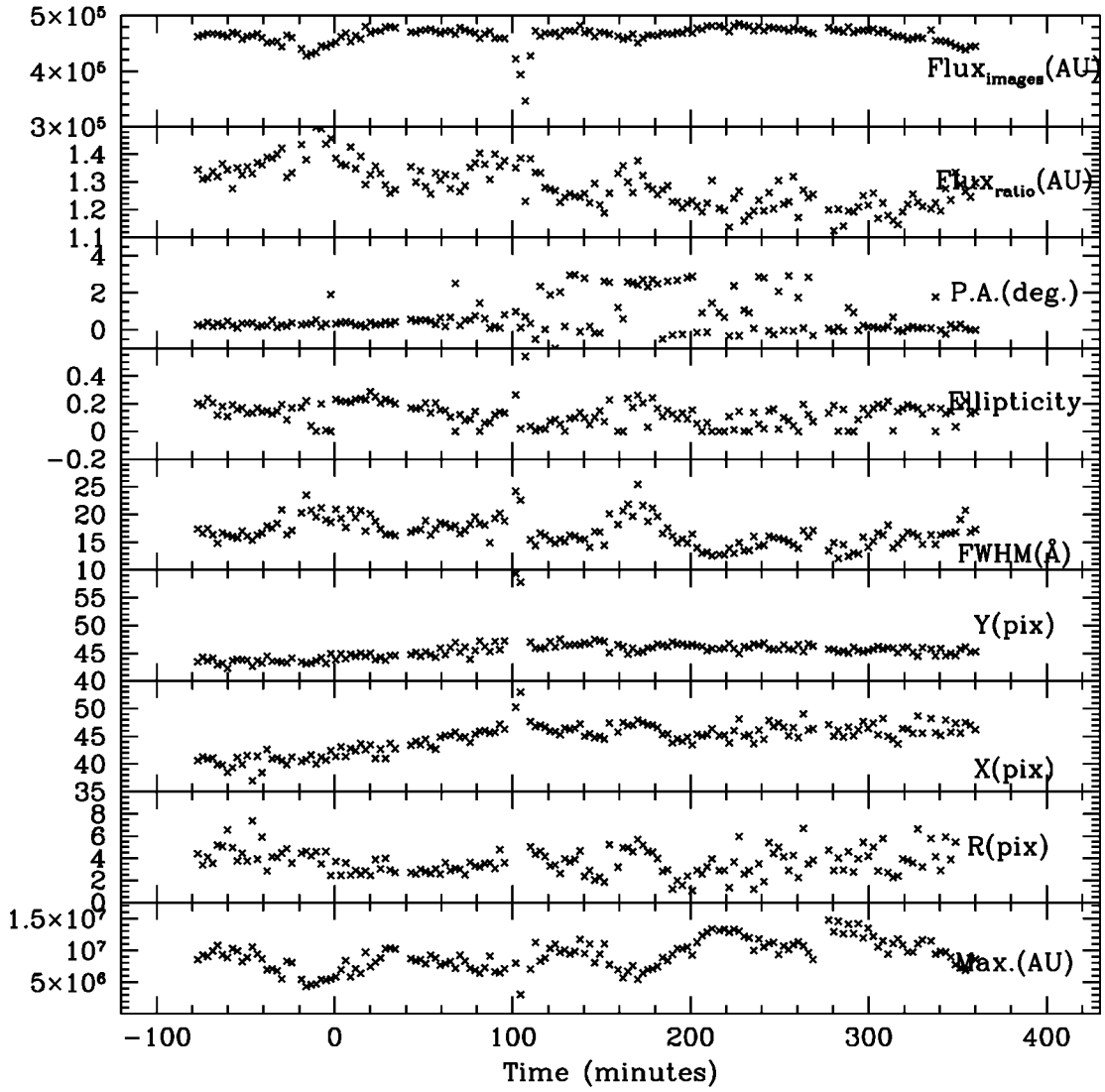

FIG. 5.—Evolution during the night for some variables inferred from Gaussian fits to the reconstructed images (see text). *Bottom to top*: (1) value of the Gaussian peak, (2) distance to fiber 111, (3) shift along the R.A. direction, (4) shift along the decl., (5) FWHM of the Gaussian fit, (6) ellipticity of the Gaussian fit, (7) P.A. of the major axis, (8) ratio between the flux contained in the seven brightest fibers vs. that contained in the 37 selected fibers, and (9) total flux in the images after interpolation. Units of vertical axis in (1), (3), and (4) refer to pixels in the interpolated image (1 pixel = 0.″05). Units for the horizontal axis are in minutes from the center of the transit. AU refers to arbitrary units.

and therefore it is not affected by motions of the rotator. In any case, and in order to check instrumental stability, we have displayed in Figure 4 the fluxes in the bands f_1, f_2, and f_3 as a function of time. No apparent differences among these three plots can be directly observed, ruling out instrumental variations in flux of the order of 5%–10%, as reported by other authors. In the top panel of Figure 4, we have also represented the ratio f_1/f_3, which has the expected much lower (<1%) variation with time (i.e., air mass), due the differential atmospheric extinction between the two bands.

From equation (1) we can determined how relative changes in f_2 translate into relative changes in I. Specifically,

$$\frac{\Delta I}{I} = \frac{-2(f_1 + f_3)f_2}{(f_1 + f_2 + f_3)(f_1 + f_3 - f_2)} \frac{\Delta f_2}{f_2}, \tag{2}$$

and taking into account that $f_1 \approx f_3 \approx 4f_2$,

$$\frac{\Delta I}{I} \approx -0.25 \frac{\Delta f_2}{f_2}. \tag{3}$$

Thus, a relative change of the flux in the Na D band translates

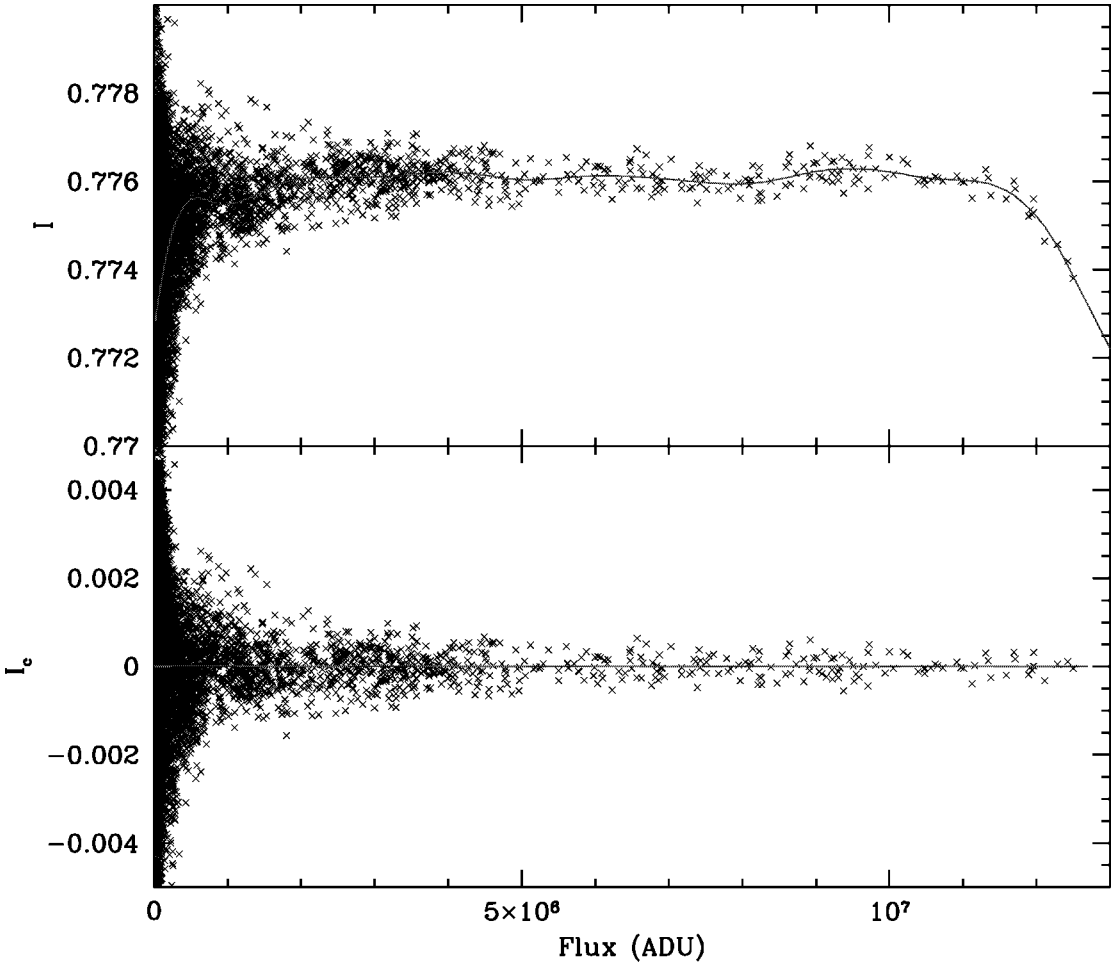

FIG. 6.—*Top*: Distribution of the photometric index as a function of the total flux (i.e., $f_t = f_1 + f_2 + f_3$) for the 5254 spectra. Red line indicates the mean systematic behavior. *Bottom*: Same distribution after removing the mean systematic behavior (see text). [*See the electronic edition of the PASP for a color version of this figure*.]

into a relative change ~4 times smaller for the index, with the opposite sign. So, taking into account the fact that in a typical exposure we collect about 7.15×10^6 e^- in f_2, the standard deviation due to photon noise for f_2 would be 3.74×10^{-4}, and therefore for the index, I should be $\sim 9.5 \times 10^{-5}$.

In addition to the index as defined above, we also evaluated a "control" index using the same definition as in equation (1), but a relatively line-free band for f_2. Specifically, the bands selected for f_1, f_2, and f_3 were 590.300–595.146, 595.146–596.454, and 596.454–601.300 nm, respectively.

5.3. Autocalibration

The index as defined above was calculated for the 37 brightest spectra of each exposure. We excluded the four exposures for which we lost the autoguiding lock, and also the four exposures taken at air masses higher than 2. The resulting 5254 values (37 spectra × 142 exposures) are represented in Figure 6 (*top*) versus the total flux in the band (i.e., $f_t = f_1 + f_2 + f_3$). Clearly, there are some systematic deviations from the expected behavior in the case that noise was only due to photon noise. This is particularly obvious for the largest f_t values, which are clearly affected by nonlinearities. At the lowest flux levels, the deviations cannot be explained by the expected systematic trend in a ratio due to statistical errors. They are likely due to a small, constant background noise due to scattered light, and perhaps some nonlinearity residuals too. In any case, these effects can be well calibrated by using the data themselves (i.e., "autocalibration"). To this aim, we fit all the data points to a smooth function (16th order spline3) of the total flux $I_{\rm fit}(f_t)$, and we redefine the index as $I_c = I - I_{\rm fit}(f_t)$. The corrected photometric index I_c for the 5254 spectra are represented as a function of the total flux in Figure 6 (*bottom*). These new I_c values should be free of the nonlinearity residuals mentioned above, since the dependence on f_t has been removed.

The distribution of values in Figure 6 was also used to check and select the proper methodology during the reduction process.

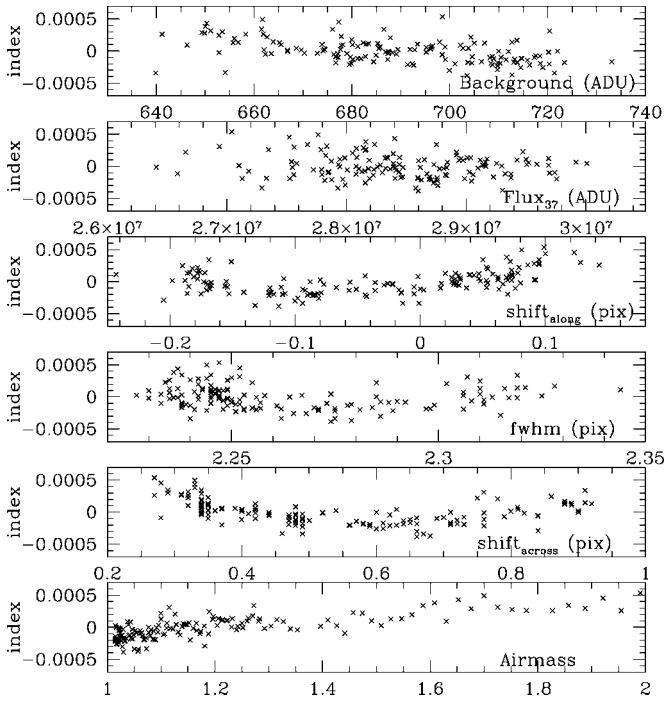

FIG. 7.—Variation of the index I_c as a function of several auxiliary variables. ADU refers to counts on the detector.

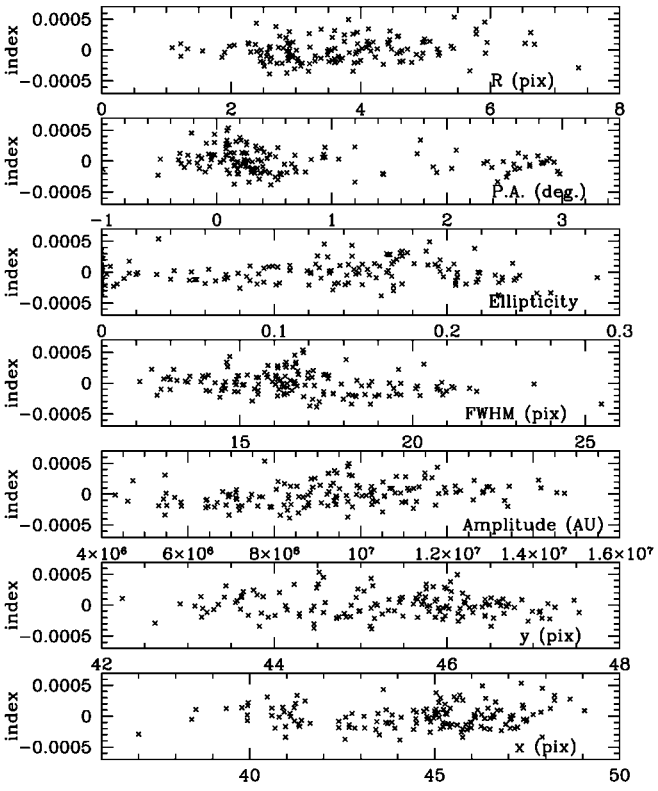

FIG. 8.—Variation of the index I_c as a function of several auxiliary variables. The units of pixels indicated in several panels correspond to pixels in the reconstructed image, which have a scale of 0.″05 pixel^{-1}. The variable R (*top*) indicates the distance of the Gaussian peak to the center of fiber number 111 (i.e., closest to the intensity peak). AU refers to arbitrary units.

For instance, we studied the effects of resampling the spectra to a common pixel-wavelength solution by analyzing the scatter in this figure. It was found that the scatter was appreciably larger when the spectra were resampled. This plot was also used to check the importance of the flat-field and linearity corrections. It was found that such corrections do indeed improve the quality of the results (i.e., the scatter in Fig. 6 is reduced), but by relatively modest amounts.

The next step was to obtain the photometric index value for each exposure (time) I'. This was done by averaging the 37 contemporaneous individual values obtained in each exposure. We use an inverse variance weighting of the index (which is proportional to the total flux f_t) in order to take into account the statistical errors of each individual I_c^i value. Therefore,

$$I' = \frac{\Sigma I_c^i \times f_t^i}{\Sigma f_t^i}, \tag{4}$$

where the subindex i runs over the 37 spectra obtained simultaneously in each exposure, and f_t^i is the corresponding total flux (in photoelectrons).

Note that apart from the possibility of performing the linearity calibration mentioned above, this procedure for generating the index is more advantageous than adding all the 37 spectra and generating the index from the combined spectrum, in terms of the influence of backgrounds (i.e., sky, scattered light, etc.), since these are actually weighted by the importance of each spectrum in the generation of the index at any given time. In addition, this method is also less sensitive to the actual spatial extent used (i.e., number of fibers involved). Thus, if for instance more than 37 fibers were used, the extra spectra would have had very little effect on I', because of their low flux.

Figures 7 and 8 show the dependence of the index on some of the auxiliary variables. In Table 1 the degree of correlation is indicated in column (4). Figure 7 and Table 1 show that the strongest correlation (0.76) is found with air mass (which contrasts with the weak anticorrelation [−0.19], shown by the "control index," when f_2 is defined outside the Na D lines, as indicated in § 5.2). Initially, we considered the possibility that this strong correlation between the index and the air mass could be due to geographical and temporal variations of the emission spectrum of the Na D lines produced in the Earth's atmosphere. However, the emission spectrum has a very small contribution, compared to the signal. In fact, considering a typical sky brightness of $V = 21.8$ mag arcsec^{-1} for La Palma, an equivalent width for the telluric emission of Na D of ~150 Å (Benn & Ellison 1998; Pedani 2004), and the parameters used in our experiment (e.g., a width of $f_2 \sim 15$ Å, a fiber collecting area

TABLE 1
DECORRELATION PARAMETERS

Number (1)	Variable (2)	Coefficient (3)	Error (4)	Correlation (5)	Conservation Factor (6)
1	Air mass	1.074	5.41E−04	0.76	0.88
2	Total flux	8.69E−04	1.33E−10	−0.14	0.88
3	Background	7.74E−02	−6.61E−07	−0.48	0.75
4	Spectra shift (along dispersion)	2.11	4.64E−04	0.38	0.33
5	Spectra shift (across dispersion)	1.60	3.60E−04	−0.29	0.32
6	Spectra FWHM	3.16	−1.87E−05	−0.11	0.38
7	Image total flux	5.82E−03	−1.01E−08	−0.16	0.88
8	Flux ratio	1.68	−5.12E−04	−0.32	0.56
9	Gaussian peak	4.55E−04	−6.08E−11	0.27	0.77
10	Gaussian *X*	0.330	−2.81E−06	8.9E−02	0.40
11	Gaussian *Y*	0.480	3.20E−05	−6.3E−02	0.46
12	Distance to fiber 111	0.384	3.24E−05	0.17	0.99
13	Gaussian FWHM	0.422	−5.55E−05	−0.27	0.84
14	Gaussian ellipticity	1.59	6.51E−04	2.3E−03	0.85
15	Gaussian P.A.	0.320	−3.57E−06	−0.19	0.94
All					0.17
1+12+13					0.79

$\sim$0.16 arcsec^{-2}, etc.), one should collect more than 10^5 photons from HD 209458 for each photon coming from the Na D emission lines. On the other hand, Charbonneau et al. (2002) have shown that the expected drop in the Na D band during the transit is $\sim 2.3 \times 10^{-4}$. Therefore, the amount we expect to detect during the transit is much larger (by at least 1 order of magnitude) than that due to the sky emission (the difficulty, of course, is in recording that signal on top of the photon noise generated by the star). Therefore, the strong correlation between the index and the air mass is likely to be dominated by the absorption produced by the Earth's atmosphere. The fact that the index has a relatively strong correlation with air mass (which obviously changes with time) may produce correlations with other variables that show a temporal variation but have no causal connection.

5.4. Decorrelation

"Decorrelation" is the process of removing trends in the index that are correlated with the auxiliary variables. This was based on a multiple-regression (least-squares) fit to the data with a function that is linear in the coefficients of independent variables, following the prescriptions given by Bevington (1969). Column (4) of Table 1 shows the correlation parameter for the 15 selected auxiliary variables. In order to have an idea of the effects of the decorrelation procedure in reducing noise, we can compare the global standard deviation of the 142 data values before (1.85×10^{-4}) and after (1.11×10^{-4}) this procedure was applied. Note that the standard deviation of the decorrelated values is remarkably close to the one expected in a purely photon-noise–dominated regime. In fact, considering a typical level of counts per exposure of 3.1×10^6 ADU (counts) for f_2, a gain of 2.3 e^- ADU^{-1}, and equation (3), a standard deviation of the index of $\sim 0.95 \times 10^{-4}$ is expected in a photon-noise–dominated regime. (It is interesting to note that the fact that the decorrelated signal shows a standard deviation close to that due to the photon noise suggests that the modal noise is very small or that it can be well tracked by the selected variables).

As we can see in Table 1, the air mass is the variable that shows the highest correlation with the index. If the data are only decorrelated linearly against the air mass (i.e., if only the linear trend observed in the bottom panel of Fig. 7 is removed), the standard deviation is 1.20×10^{-4}. If we decorrelate against all other variables but exclude the air mass, the standard deviation is 1.17×10^{-4}. In Figure 9 (*left column*), we show the original data (*top*), the fit to a function that is linear to the air mass (*middle*), and the decorrelated data (*bottom*), as a function of time. The center and right columns of Figure 9 are similar, but the data are fitted to a function that is linear to 14 variables (all but the air mass) and to all 15 selected auxiliary variables, respectively. It is interesting to note how the rest of the variables also carry information about the effects of the air mass.

If we select for decorrelation the six auxiliary variables derived from the spectra (background, shift in *x*, shift in *y*, FWHM, ΔFWHM, and total flux), the standard deviation is 1.39×10^{-4}. If we select the nine variables from the images (background, peak, shift in *x*, shift in *y*, distance to central fiber [number 111], FWHM, ellipticity, P.A., and total flux), the standard deviation drops to 1.24×10^{-4}. This illustrates one of the advantages of using IFS: having control of the image characteristics at the focal plane offers the possibility of improving the photometry by removing correlated noise.

Although this decorrelation method can be applied safely if the functional dependence of the auxiliary variables are different from that of the signal to be detected, it may destroy part of it when that is not the case. This is more likely when many different variables are involved in the decorrelation process. In addition, the fact that our observations include only

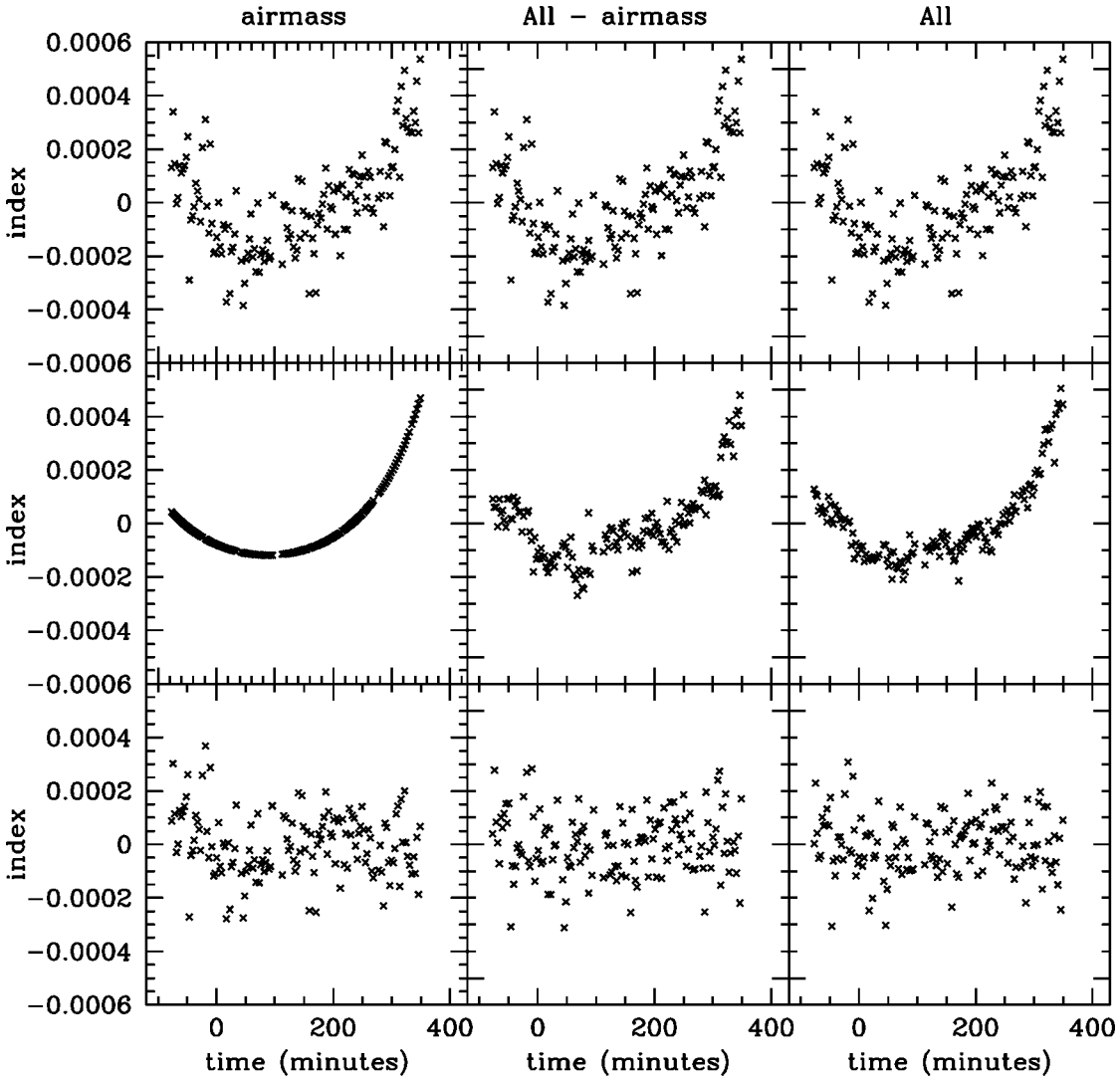

FIG. 9.—Temporal variation of the index I_c. The top panels indicate the original distribution of values. Middle panels represent the fit of the original distribution to a linear function in the variables indicated at top (i.e., air mass [*left*], the 15 variables described in Table 1, excluding the air mass [*center*], and the 15 variables [*right*]). The bottom panels show the decorrelated distribution, which is obtained by subtracting the fit to the original values. The standard deviation for these distributions are 1.2×10^{-4} (*left*), 1.15×10^{-4} (*center*), 1.1×10^{-4} (*right*). Units for the horizontal axis are in minutes from the center of the transit.

one transit, and that this represents a relatively large fraction (~30%) of the whole observed period, makes this possibility more likely. Ideally, observations during long out-of-transit periods will characterize more accurately the dependence on the variables. Obviously, having data for multiple transits will minimize the possible artificial attenuation of the signal during the transit. In any case, to study the degree of destruction of the signal during the transit due to the decorrelation process, we proceed as follows. Similarly to Brown et al. (2002), we injected an artificial signal into the data (during the period that the transit took place) before the decorrelation was applied, and we analyzed how much of this signal was recovered after decorrelation. First, the effects of each auxiliary variable were analyzed individually. This was done by comparing the input and output signals after decorrelating against each of the 15 variables. Column (5) in Table 1 indicates the fraction of signal recovered when the decorrelation is done using only this variable. In an attempt to estimate the error for these conservation factors, we used different levels of injected artificial signal (i.e., 0.5, 1, and 2 times the expected change, according to the *HST* STIS result), but the conservation factors were similar for these three cases. Table 1 shows that in several cases, more than 80% of the signal is recovered, while in other cases, this is less than 30%. This is the case for three variables inferred from the spectra (shift in x, shift in y, and FWHM). This is likely due to their monotonic behavior through the night; something that

can mimic a transit occurred during the first part of the night, as it was in the present case. However, a variable with a different type of dependence, such as the air mass (which decreases and increases through the night, with the inflexion point offset with respect to the transit), better preserves the signal. During the 132 minutes considered as in-transit observations (i.e., excluding the ingress and egress), the air mass changed from 1.242 to 1.019. However, after the pass through the meridian, the change in air mass from 1.019 to 1.242 (and on) was done out-of-transit. We then studied the combined effects of several variables. We found that when all 15 variables are used to remove noise (i.e., decorrelation process), most of the signal was actually destroyed: only 17% of the signal that is artificially injected is recovered after decorrelation.

The next step in the analysis was to select a subset of auxiliary variables that would lead to a significant reduction of noise while preserving a substantial fraction of the signal. After several trials based on the individual destruction factors, we found that three variables (air mass, FWHM of the image, and distance to fiber 111) give a good compromise. Specifically, the standard deviation of the 142 points was 1.19×10^{-4}, while 79% of the signal is preserved after decorrelation. Although the addition of FWHM and distance to fiber 111 implies a relatively modest improvement in the standard deviation with respect to the decorrelation against the air mass only, these variables were included because they take into account the position and shape of the image on the fiber bundle, which show a relatively strong correlation with the total flux (see Fig. 5). In any case, we checked that this selection did not affect our results, and values after decorrelating against the air mass only are given hereafter.

At this point we evaluated the effects of the autocalibration (see § 5.3) on the final standard deviation. If the decorrelation procedure is applied to the data without applying the autocalibration step, a standard deviation of 1.25×10^{-4} is obtained. (Values for which the total flux f_t was larger than 1.18×10^7 were excluded, since they show saturation; see Fig. 6). This demonstrates that the autocorrelation step allows us to improve the photometric accuracy and to recover some of the saturated values (improving the temporal coverage and the error of the mean value).

5.5. Time Series

Figure 10 (*top*) shows the time-series data. Vertical lines indicate the contacts. Following Charbonneau et al. (2002), we define in-transit observations as those that occurred between second and third contact (i.e., $|t - T_c| < 66.1$ m), and out-of-transit observations as those that occurred before the first or after the fourth contact (i.e., $|t - T_c| > 92.1$ m). There are 45 in-transit observations and 84 out-of-transit observations, ignoring those observations that occurred during ingress and egress.

As mentioned above, the standard deviation of all 142 values

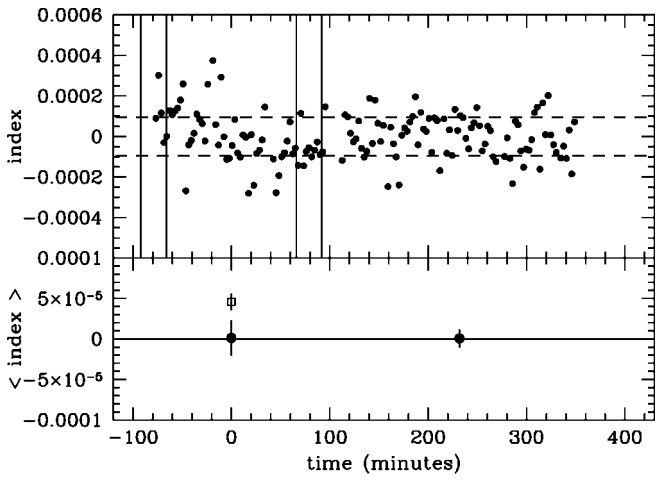

FIG. 10.—*Top*: Temporal variation of the index I_c after decorrelation with three selected variables (air mass, image FWHM, and distance to fiber 111). Vertical lines indicate (*from left to right*) first, second, third, and fourth contact. Horizontal dashed lines show the expected $\pm 1\ \sigma$, according to photon noise. *Bottom*: Averaged values in-transit (i.e., between second and third contact) and out-of-transit (i.e., after fourth contact). The value corresponding to the *HST* observations by Charbonneau et al. (2002) is shown with an open square (see text).

represented in Figure 10 is 1.19×10^{-4}. However, the standard deviation in-transit (1.46×10^{-4}) is significantly larger than out-of-transit (1.03×10^{-4}). We think this is attributable to the more unstable conditions of the atmosphere/background at the beginning of the night. Although our meteorological data do not show strong evidence for that (see Fig. 3), variations of the telluric vapor absorption (e.g., Lundstrom et al. 1991) and/or of the mesospheric sodium column density (e.g., Ge et al. 1998) could produce these instabilities. In any case, it is remarkable that for out-of-transit observations, using data that expand for a period of ~4 hr, the standard deviation is very similar to that expected from Poisson noise.

Figure 10 (*bottom*) shows the mean in-transit and out-of-transit values of the index, $(0.12 \pm 2.17) \times 10^{-5}$ and $(0.06 \pm 1.12) \times 10^{-5}$, respectively. The quoted $1\ \sigma$ errors correspond to the error in the mean of the statistical distribution (i.e., standard deviation/$\sqrt{n}$). (If the index is decorrelated against the air mass only, the corresponding values are $[-0.04 \pm 2.16] \times 10^{-5}$ and $[0.16 \pm 1.13] \times 10^{-5}$, respectively.) These results are compatible with no variation of the index during the transit (i.e., the relative variation is $[0.06 \pm 2.44] \times 10^{-5}$), and taking into account equation (3), no variation of the relative flux in the Na D lines (i.e., f_2) with respect to the continuum during the transit. We also show in this figure the expected change in the index due to a change in f_2, like the one detected by *HST* STIS (Charbonneau et al. 2002). Provided that these authors found a relative change in f_2 of $(-2.32 \pm 0.57) \times 10^{-4}$ during the transit, according to equation (3), one should have expected a relative change in the index of 5.80×10^{-5} with a conser-

TABLE 2
Na D Measurements of HD 209458b

Work	Value	Band (Å)	Experimental Setup
Charbonneau et al. (2002)	$(23.2 \pm 5.7) \times 10^{-5}$	12	*HST* STIS
	$(13.1 \pm 3.8) \times 10^{-5}$	38	
	$(3.1 \pm 3.6) \times 10^{-5}$	100	
Narita et al. (2005)	$(30 \pm 40) \times 10^{-5}$	12	Subaru HDS
Present work	$(0.2 \pm 9.8) \times 10^{-5}$	15	WHT INTEGRAL

vation factor of 1, and 4.58×10^{-5} with the current conservation factor of 0.79 (see § 5.4). (This neglects the slightly different width of the 12 Å band used by Charbonneau et al. with respect to the 15 Å band used by us. This is justified by comparing their results for 12 and 38 Å bands [see Table 2]; a change of 3 Å in the band width would imply a change of $\sim 0.28 \times 10^{-5}$ in the index, about a factor of 5 smaller than the error quoted by them). Therefore, if a signal with an amplitude like the one reported by Charbonneau et al. were real, and after repeating the current experiment many times, the (Gaussian) distribution of results should peak at 4.58×10^{-5}, with a σ of 2.44×10^{-5}. However, we (and Charbonneau et al.) have performed the experiment only once, and the result obtained is about 2 σ away from the expected value (for a signal like the one detected by Charbonneau et al. data). If we take into account the quoted errors, the present data and the *HST* STIS results disagree by more than 1 σ, but they are compatible within 1.5 σ.

This limited statistical significance makes us cautious about overinterpreting the present results, which are about a factor of 2 more uncertain than the *HST* data. Since atmospheric variables, and especially the air mass, dominate the decorrelation procedure, a better knowledge of the typical timescale for variation of the differential absorption in the Na D band by the Earth's atmosphere would be useful to further analyses. However, note that we could have obtained significantly better accuracy if the atmospheric conditions during the transit were similar to those seen out-of-transit. In that case, the current 2.44×10^{-5} (1 σ) error would have dropped to 1.9×10^{-5}. In addition, multiple transit observations would lead also to a significant reduction of this error. The recent ground-based observations by Narita et al. (2005) could not confirm nor contradict the Charbonneau et al. (2002) result. Although these Subaru observations have much higher spectral resolution, its lower S/N and temporal resolution lead to an error in the predicted relative flux in Na D lines (for a 12 Å band) that is larger (by a factor of about 4) than that of the current observations.

6. CONCLUSIONS

The main conclusions of the present work can be summarized as follows.

1. We have shown that integral field spectroscopy is a powerful technique for obtaining accurate (high-S/N) relative time-series photometry; therefore, it has great potential for studying transits of extrasolar planets. The three main advantages with respect to previously used methods (based on imaging or standard slit spectroscopy) are (1) it allows an increase in the duty cycle of the observations (and therefore the S/N) by distributing the light into the two dimensions of the detector, (2) the data can be "autocalibrated" from detector nonlinearities and from background effects, and (3) since the photometric index, the image of the star (PSF), and variables accounting for instrument instabilities are extracted from the same data cube, noise in the photometric signal correlated with the PSF or the instrumental variables can be removed.

2. These observations have also allowed us to explore the accuracy limits that can be achieved from the ground for these types of observations. In particular, using a photometric index that probes the strength of the Na D lines, a standard deviation of 1.85×10^{-4} was found (during a $\sim$7 hr period), which is about a factor of 2 larger than that expected due to photon noise. However, after removing correlated noise by fitting the data to a linear function in three selected auxiliary variables, the standard deviation drops to 1.19×10^{-4}, only $\sim$25% larger than that due to photon noise. Simulations indicate that 79% of the relative flux change during the transit should be preserved after decorrelating against those three variables. Our nominal 1 σ error for the mean in-transit value (with respect to the mean out-of-transit value) for the index is equivalent to 9.7×10^{-5} for the relative flux in the Na D band (f_2) with respect to the continuum. This is substantially better than previous ground-based observations, and only a factor of $\sim$2 times worse than the four transit observations with the *HST* STIS.

3. The present mean values for the photometric index in-transit and out-of-transit are compatible with no extra depression of the Na D during the transit. Although the present results are in apparent contradiction to the *HST* STIS results, we stress the limited statistical significance of this disagreement: they disagree at 1 σ, but they are consistent within 1.5 σ. We acknowledge that our results have larger nominal errors and are more susceptible to systematically underestimating the signal through decorrelation.

4. The present study indicates that a good level of accuracy

can be obtained from the ground with this type of IFS observation. The 5254 spectra analyzed here were collected during only one night/transit and are therefore insufficient to reduce the nominal errors to the level of the four-transit *HST* STIS data. Multiple transit observations will also allow us to analyze the typical timescale variations for relevant atmospheric variables, and therefore better understand the effects of the decorrelation procedure on the photometric index.

5. From an instrument design perspective, this application of IFS can be fostered if (1) the fiber bundle (image slicer, array of microlenses) have an independent focusing mechanism, (2) direct illumination of the detector is possible for generating flat fields, and (3) the sky is simultaneously recorded. Fiber systems seem to have some generic advantages with respect to another types of IFU (e.g., azimuthal scrambling of the light within the fibers, the possibility of using static spectrographs, etc.). Furthermore, our data indicate that modal noise or the temporal variation of the fiber throughput with wavelength are not significant sources of noise.

Further multitransit observations with long out-of-transit data (ideally from space) should lead to the development of the full potential of the proposed method. For ground-based observations, the use of the recently developed new integral field spectrographs for 8 m class telescopes (e.g., GMOS: Allington-Smith et al. 2002; SINFONI/SPIFFI: Eisenhauer et al. 2003, VIMOS: Le Fevre et al. 2003) will permit us to develop the present technique.

We are grateful to Chris Benn, Ivo Busko, Katrina Exter, Phill Hodge, Danny Lennon, Jesús Maíz-Apellániz, and Simon Tulloch, who have provided us with useful information. We also thank the anonymous referee for useful comments.

This paper is based on observations made with the WHT, operated on the island of La Palma by the ING in the Spanish Observatorio del Roque de los Muchachos of the Instituto de Astrofísica de Canarias. We thank all the staff at the observatory for their kind support. Support for this work was also provided by the Spanish Ministry of Education and Science through grant AYA2002-01055.

REFERENCES

Allington-Smith, J. R., et al. 2002, PASP, 114, 892
Arribas, S., & Mediavilla, E. 2000, in ASP Conf. Ser. 195, Imaging the Universe in Three Dimensions, ed. W. van Breugel & J. Bland-Hawthorn (San Francisco: ASP), 295
Arribas, S., Mediavilla, E., & Fuensalida, J. J. 1998a, ApJ, 505, L43
Arribas, S., et al. 1998b, Proc. SPIE, 3355, 821
Baudrand, J., & Walker, G. A. H. 2001, PASP, 113, 851
Benn, C. R., & Ellison, S. L. 1998, NewA Rev., 42, 503
Bevington, P. R. 1969, Data Reduction and Errror Analysis for the Physical Sciences (New York: McGraw-Hill)
Bingham, R. G., Gellatly, D. W., Jenkins, C. R., & Worswick, S. P. 1994, Proc. SPIE, 2198, 56
Borucki, W., et al. 2004, in Second Eddington Workshop, Stellar Structure and Habitable Planet Finding, ed. F. Favata, S. Aigrain & A. Wilson (ESA SP-538; Noordwijk: ESA)
Brown, T. M. 2001, ApJ, 553, 1006
Brown, T. M., Charbonneau, D., Gilliland, R. L., Noyes, R. W., & Burrows, A. 2001, ApJ, 552, 699
Brown, T. M., Libbrecht, K. G., & Charbonneau, D. 2002, PASP, 114, 826
Bundy, K. A., & Marcy, G. W. 2000, PASP, 112, 1421
Charbonneau, D., Brown, T. M., Noyes, R. W., & Gilliland, R. L. 2002, ApJ, 568, 377
Charbonneau, D., et al. 2000, ApJ, 529, L45
Coustenis, A., et al. 1998, in ASP Conf. Ser. 134, Brown Dwarfs and Extrasolar Planets, ed. R. Rebolo, E. L. Martin, & M. R. Zapatero Osorio (San Francisco: ASP), 296
Deeg, H. 2002, in 36th ESLAB Symposium, ed. B. Foing & B. Battrick (ESA SP-514; Noordwijk: ESA), 237
del Burgo, C., Mediavilla, E., & Arribas, S. 2000, ApJ, 540, 741
Deming, D., Brown, T. M., Charbonneau, D., Harrington, J., & Richardson, L. J. 2005, ApJ, 622, 1149
Deming, D., Seager, S., Richardson, L. J., Harrington, J., 2005, Nature, 434, 740
Dhillon, V., & Marsch, T. 2002, Newsl. Isaac Newton Group Telesc., 6, 25
Eisenhauer, F., et al. 2003, Proc. SPIE, 4844, 1548
Ge, J., Jacobsen, B. P., Angel, J. R. P., McGuire, P. C., Roberts, T., McLeod, B. A., & Lloyd-Hart, M. 1998, Proc. SPIE, 3353, 242
Gilliland, L. R., & Arribas, S. 2003, High Signal-to-Noise Differential NICMOS Spectrophotometry (ISR-NICMOS-03-01; Baltimore: STScI)
Gilliland, L. R., Goudfrooij, P., & Kimble, R. A 1999, PASP, 111, 1009
Henry, G. W., Marcy, G. W., Butler, R. P., & Vogt, S. S. 2000, ApJ, 529, L41
Le Fevre, O., et al. 2003, Proc. SPIE, 4841, 1670
Lundstrom, I., Ardeberg, A., Maurice, E., & Lindgren, H. 1991, A&A, 91, 199
Mazeh, T., et al. 2000, ApJ, 532, L55
Moutou, C., Coustenis, A., Schneider, J., St Gilles, R., Mayor, M., Queloz, D., & Kaufer, A. 2001, A&A, 371, 260
Narita, N., et al. 2005, PASJ, 57, 471
Pedani, M. 2004, NewA, 9, 641
Rauer, H., Bockelée-Morvan, D., Coustenis, A., Guillot, T., Schneider, J. 2000, A&A, 355, 573
Sparks, W. B., & Ford, H.C. 2002, ApJ, 578, 543
Tulloch, S. 2001, Isaac Newton Group Tech. Note, 119
Vidal-Madjar, A., et al. 2003, Nature, 422, 143
———. 2004, ApJ, 604, L69
Winn, J. N., Suto, Y., Turner, E. L., Narita, N., Frye, B. L., Aoki, W., Sato, B., & Yamada, T. 2004, PASJ, 56, 655